LETTER

doi:10.1038/nature13461

Quasiparticle engineering and entanglement propagation in a quantum many-body system

P. Jurcevic[1,2]*, B. P. Lanyon[1,2]*, P. Hauke[1,3], C. Hempel[1,2], P. Zoller[1,3], R. Blatt[1,2] & C. F. Roos[1,2]

The key to explaining and controlling a range of quantum phenomena is to study how information propagates around many-body systems. Quantum dynamics can be described by particle-like carriers of information that emerge in the collective behaviour of the underlying system, the so-called quasiparticles[1]. These elementary excitations are predicted to distribute quantum information in a fashion determined by the system's interactions[2]. Here we report quasiparticle dynamics observed in a quantum many-body system of trapped atomic ions[3,4]. First, we observe the entanglement distributed by quasiparticles as they trace out light-cone-like wavefronts[5–11]. Second, using the ability to tune the interaction range in our system, we observe information propagation in an experimental regime where the effective-light-cone picture does not apply[7,12]. Our results will enable experimental studies of a range of quantum phenomena, including transport[13,14], thermalization[15], localization[16] and entanglement growth[17], and represent a first step towards a new quantum-optic regime of engineered quasiparticles with tunable nonlinear interactions.

Experimental study of the quantum coherent properties of quasiparticles represents a significant challenge over a broad range of disciplines, from investigating the propagation of quantum correlations by magnons or phonons in naturally occurring systems, to creating exotic anyons in engineered quantum matter for topological quantum technology[18]. Very recently, in an engineered system of 10 to 18 atoms in an optical lattice[9,10], the propagation of correlations by magnons was observed. Detecting the quantum nature of the correlations distributed by quasiparticles (that is, entanglement) has not yet been achieved.

We present experiments in an engineered one-dimensional system of atomic ions, whose dynamics are accurately described by a lattice model of interacting spins. The salient features of our system are as follows: first, we are able to inject localized excitations into the system and, in the subsequent dynamics, measure arbitrary multi-particle correlation functions, thereby allowing the possibility of detecting and quantifying entanglement. Second, we can tune the ion–ion interaction range from effectively nearest-neighbour to infinite range. In each case, a new set of quasiparticles is created with unique dynamical properties. In contrast to quantum simulation, where one aims to study computationally complex processes, our goal is to manipulate individual quasiparticles and their properties precisely, and observe the information and quantum correlations that they transport.

In any quantum system with finite-range interactions (for example, nearest-neighbour), quasiparticles have a finite maximal velocity, known as the Lieb–Robinson velocity[5,19,20]. Such systems exhibit an effective light cone for quantum dynamics that strictly bounds the speed with which information propagates, as recently observed[9,10]. However, many natural and engineered quantum systems exhibit long-range interactions that decay as a power law, such as dipole–dipole or van der Waals interactions. Understanding the quantum dynamics in this more general case is an active field of theoretical research[12,17,21,22]. For weakly long-range interactions, the light-cone picture remains a good description, but as the interaction range increases, the maximal velocity in the system is predicted to diverge and the light-cone picture no longer applies[12]. Here, we experimentally access these regimes.

We control the quantum state and interactions of the valence electron in each ($^{40}Ca^{+}$) ion, which can be in one of two states $|S_{1/2},m=+1/2\rangle$ or $|D_{5/2},m=+5/2\rangle$ that we label $|\downarrow\rangle$ and $|\uparrow\rangle$ respectively. The quasiparticles of our system are therefore collective electronic excitations. In the presence of laser-driven interactions, our system is well described by a one-dimensional model of interacting spins, with Hamiltonian[3,4]

$$H_{\mathrm{Ising}}=\hbar\sum_{i<j}J_{ij}\sigma_i^x\sigma_j^x+\hbar B\sum_i\sigma_i^z$$

where $\hbar=h/2\pi$, $\sigma_i^{\beta}(\beta=x,y,z)$ are the spin-1/2 Pauli operators for the ith spin and B is an effective transverse magnetic field strength. The coupling matrix $J_{ij}\propto 1/|i-j|^{\alpha}$ has an approximately power-law dependence with distance $|i-j|$, with an exponent tunable between infinite range $(\alpha=0)$ and short range $(\alpha=3)$. Previous trapped ion experiments[23–25] have investigated the ground state properties of H_{Ising}. Here, we investigate out-of-equilibrium dynamics and a new regime where $B\gg\max(|J_{ij}|)$. In this case, the number of spin excitations $(\uparrow_z)$ is conserved during the dynamics, and H_{Ising} reduces to the XY model of hopping hard-core bosons, $H_{XY}=\hbar\sum_{i<j}J_{ij}\left(\sigma_i^{+}\sigma_j^{-}+\sigma_i^{-}\sigma_j^{+}\right)$. For further experiment details, see Methods.

Using a tightly focused laser and single-ion resolved imaging, we can inject localized excitations and observe the system's response. These local quenches (that is, sudden perturbations of the system) allow the dynamical properties of individual quasiparticle wave-packets to be studied, in particular their dispersion relation and entanglement distribution. Local quenches are performed by flipping one or more spins, thus coherently populating a range of quasiparticle modes. Each mode can be pictured as an equal superposition of spin waves (magnons) with positive and negative momentum $\pm k$. Therefore, in the subsequent time evolution, superpositions of left-travelling and right-travelling spin waves, ejected from the quench site, distribute entanglement amongst the spins (Fig. 1a).

The precise dynamics are determined by the quasiparticle dispersion relation, which in turn can be tuned by the spin–spin interaction range[12]. We can verify the correct implementation of the desired interaction range and the corresponding quasiparticle dispersion relation by directly measuring the spatial distribution of the spin–spin interactions (Fig. 1b). The measurement closely matches theoretical predictions (see Extended Data Fig. 5). Fitting a dispersion relation from power-law interactions allows us to extract the exponent α (Fig. 1c).

The spread of information from the local quench sites can be observed in spatially and temporally resolved single-spin observables, such as the spin polarization $\langle\sigma_i^z(t)\rangle$, which characterizes the magnetization of the system (Fig. 2a–c). At early times, localized spin-wave packets radiating away from single spin-excitations are clearly visible. Later, reflections result in complex interference patterns, with properties determined by both α and the spin chain length. Questions such as whether the initially

[1]Institut für Quantenoptik und Quanteninformation, Österreichische Akademie der Wissenschaften, Technikerstraße 21a, 6020 Innsbruck, Austria. [2]Institut für Experimentalphysik, Universität Innsbruck, Technikerstraße 25, 6020 Innsbruck, Austria. [3]Institut für Theoretische Physik, Universität Innsbruck, Technikerstraße 25, 6020 Innsbruck, Austria.
*These authors contributed equally to this work.

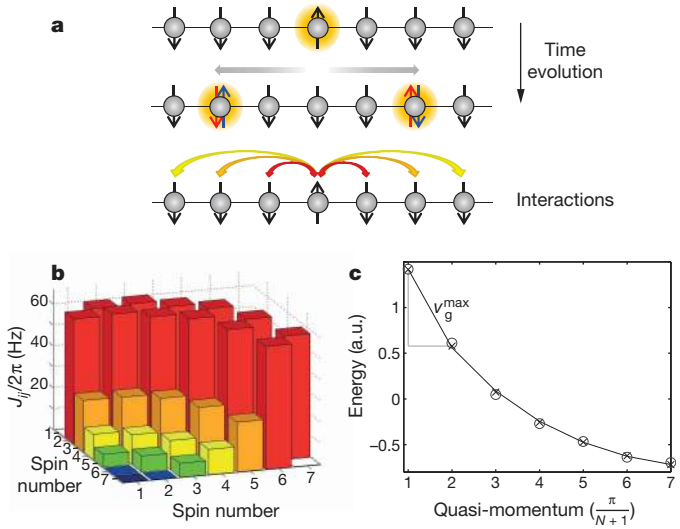

Figure 1 | Quantum dynamics in a one-dimensional spin chain following a local quench. **a**, A steady state is locally perturbed by flipping one spin. Quasiparticle wave-packets propagate left and right from the quench site and entangle spin pairs across the system. The underlying spin–spin interaction defines possible direct hopping paths (examples shown as arrows) and the quasiparticle dispersion relation. **b**, Example of a long-range spin–spin interaction matrix J_{ij}, directly measured in our system for $N = 7$ spins (see Methods), with colours matched to the interactions pictured in **a**. **c**, Quasiparticle dispersion relation (shifted by energy B), derived from **b** (circles) and predicted using experimental parameters (crosses). The line is the fitted dispersion relation for power-law interactions, with best-fit exponent $\alpha = 1.36$. The maximum group velocity v_g^{max} is inferred from the curve's steepest slope (we set the lattice spacing to unity). a.u., arbitrary units. Error bars (1σ) are smaller than symbols used.

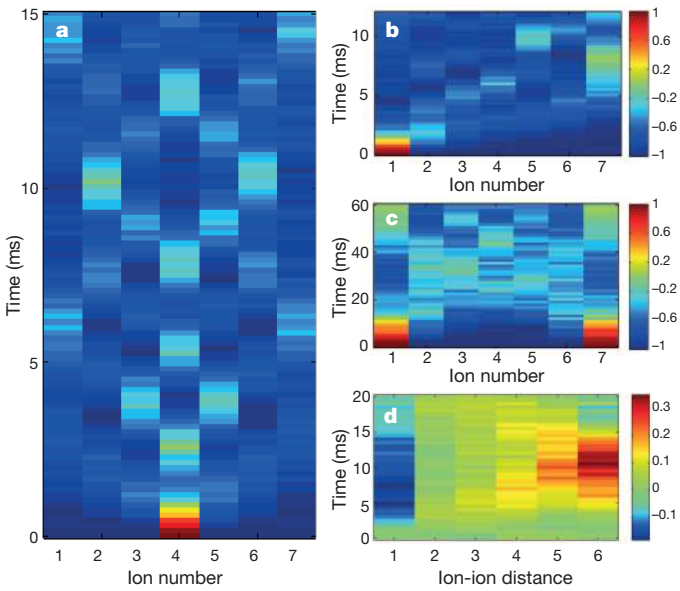

Figure 2 | Measured quantum dynamics in a seven-ion system following local and global quenches. **a**–**c**, Time evolution of the magnetization $\langle \sigma_i^z(t) \rangle$ (colour coded) following a local quench at: **a**, the central spin (ion), for $\alpha \approx 1.36$; **b**, the leftmost spin, for $\alpha \approx 1.36$; and **c**, both ends of the chain, for $\alpha \approx 1.75$. Values of ± 1 correspond to the fully polarized states. The colour scales in **b** and **c** also refer to **a**. **d**, Time evolution of the averaged two-spin correlation function $\overline{C}_n = \frac{1}{N-n} \sum_i^{N-n} C_{i,i+n}$ (colour coded) where $C_{i,j} = \langle \sigma_i^z \sigma_j^z \rangle - \langle \sigma_i^z \rangle \langle \sigma_j^z \rangle$ following a global quench, for $\alpha \approx 1.75$. The timescales (in units of $1/J$, where $J = \sum_i J_{i,i+1}/(N-1)$ so that the time evolution can be compared with different values of α) are for **a**–**d**, respectively: $T_{max} = 8.36, 6.72, 5.44, 3.12$.

localized excitation refocuses are non-trivial even in the simpler case of nearest-neighbour interactions[13].

Flipping several spins at both ends of the chain creates counter-propagating wavefronts, opening the prospect of studying quasiparticle collisions (Fig. 2c). Extended Data Fig. 1 shows close agreement with theory in all cases. Initializing all N spins in $|\downarrow\rangle + |\uparrow\rangle$ realizes a global quench. In this case, the many-body state is in a superposition containing 0 through to N excitations, in which interactions between single-excitation quasiparticle modes can no longer be neglected. In this case, the resulting distribution of information can be observed through two-point correlation functions[9,26], as seen in Fig. 2d and Extended Data Fig. 2.

To reveal the distribution of quantum correlations after a local quench, we tomographically measure the evolution of the full quantum state of pairs of spins (see Fig. 3 and Extended Data Fig. 3). Figure 3a exemplifies the results for an interaction range $\alpha \approx 1.75$, for which a clear wavefront is apparent. The results show that magnon wave-packets emerging from either side of the initial excitation distribute entanglement across the spin chain (Fig. 3b, c); the wavefront first entangles spins neighbouring the quench site, then the next-nearest neighbours, and so on until the boundaries are reached.

Finally, we investigate how the spin–spin interaction range affects the way in which information is transported around the system. For this, we measure the magnetization dynamics following a local quench in a chain of 15 spins, for three values of α roughly equally spaced around $\alpha = 1$. In the shortest-range case (Fig. 4a, $\alpha = 1.41$), an approximate light cone can be seen. There is a clear leading wavefront of spin-excitation that moves away from the quench site at a well defined velocity, and outside which the signal decays rapidly (Fig. 4a, d). These are the features of a well-defined speed limit for quantum dynamics that one would expect for finite-range interactions, and that has previously been observed in systems of neutral atoms with nearest-neighbour interactions[9,10]. Indeed, the information transport observed in our shortest-range experiment is largely captured by a Lieb–Robinson bound that considers only the nearest-neighbour interactions in the system (Fig. 4a, d, e).

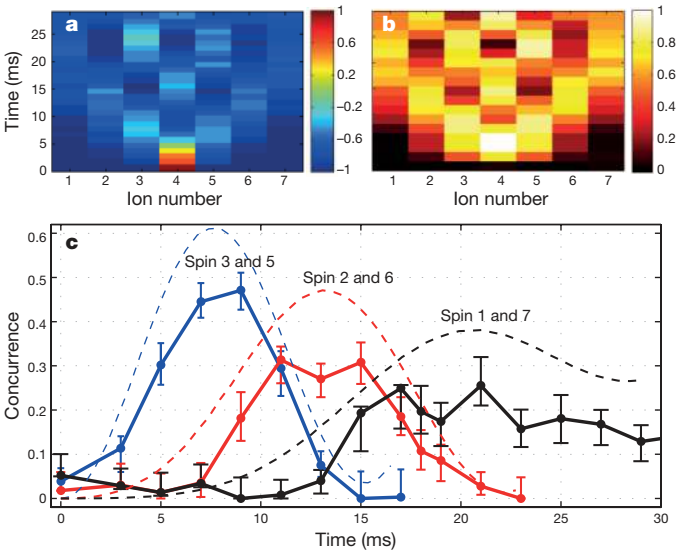

Figure 3 | Entanglement distribution following a local quench. Shown are the dynamics for $\alpha \approx 1.75$ up to $T = 30$ ms ($2.99 J^{-1}$). **a**, Measured single-spin magnetization (colour coded). **b**, Single-spin von Neumann entropy $-\mathrm{Tr}(\rho \log(\rho))/\log(2)$ (colour coded) derived from measured density matrices. High-entropy states are due to correlations with other spins. **c**, Evolution of entanglement (concurrence, see Methods) between pairs of spins distributed symmetrically around the central spin, revealing the propagation of entangled quasiparticles from the centre to the boundaries of the system. Blue, spins 3 and 5; red, spins 2 and 6; black, spins 1 and 7. Dashed lines show theoretical predictions. Error bars, 1σ calculated via Monte Carlo simulation of quantum projection noise[30].

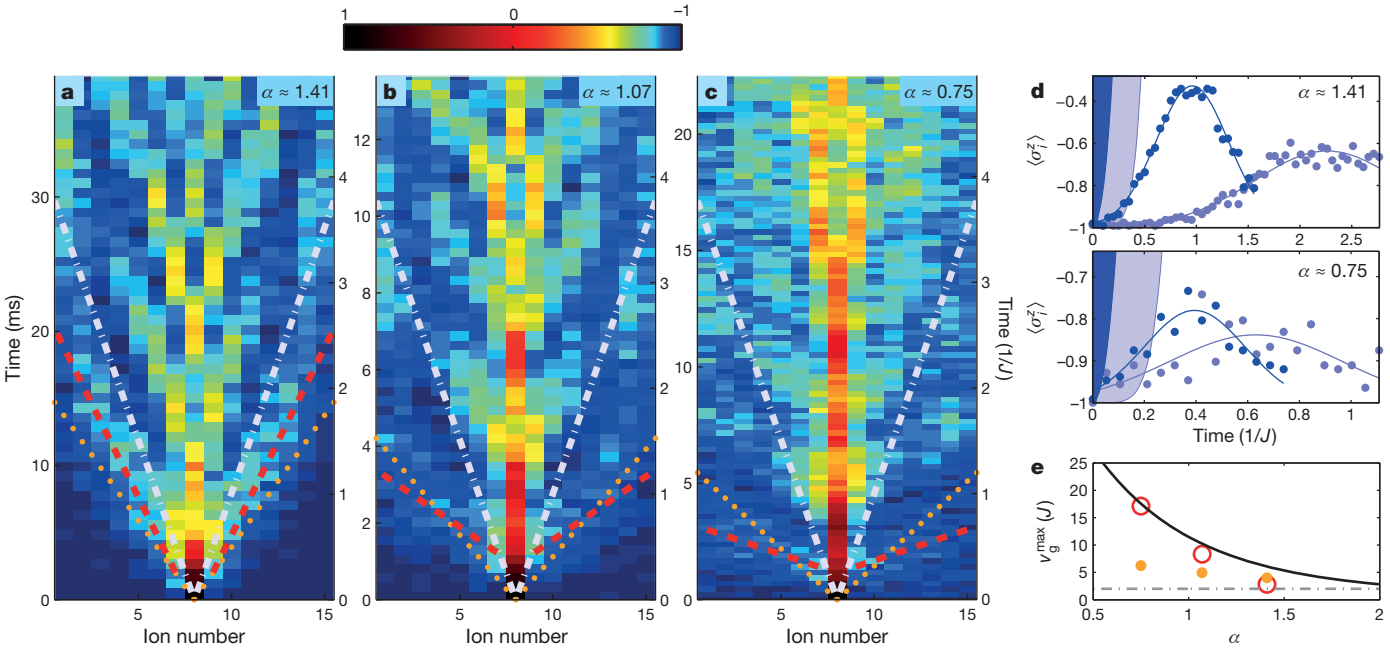

Figure 4 | Measured quantum dynamics for increasing spin–spin interaction ranges. **a–c**, Measured magnetization $\langle \sigma_i^z(t) \rangle$ (colour coded) following a local quench. From **a** to **c**, the interaction ranges are $\alpha \approx 1.41$, 1.07, 0.75. In **a**, an effective light cone is evident and the dynamics are approximately described by nearest-neighbour interactions only. Red lines, fits to the observed magnon arrival times (examples in **d**); white lines, light cone for averaged nearest-neighbour interactions; orange dots, after renormalization by the algebraic tail (see Methods). As the interaction range is increased (**b**, **c**) the light cone disappears and nearest-neighbour models fail to capture the dynamics. **d**, Magnetization of spins (ions) 6 and 13, from **a** (top) and **c** (bottom). Solid lines, Gaussian fits to measured magnon arrival. Top: for $\alpha = 1.41$, a nearest-neighbour Lieb–Robinson bound captures most of the signal (shaded region, Methods). Bottom: for $\alpha = 0.75$, it does not. **e**, Maximum group velocity. With increasing α, the measured magnon arrival velocities (red circles) approach the group velocity of the non-renormalized nearest-neighbour model (grey dash-dotted line). If renormalized by the algebraic tail, the nearest-neighbour group velocity increases at small α (orange dots), but much less than the increase of the observed magnon velocity. For small α, the measured arrival times are consistent with the divergent behaviour predicted for full power-law interactions (black line).

As the interaction range is increased (Fig. 4b, c), the arrival times of the first maxima in magnetization are seen to appear earlier and earlier, reflecting the ejection of faster and faster quasiparticles from the quench site. Furthermore, the signal decay outside these maxima is very slow: there is an almost instant increase in the magnetization even at large distances (Fig. 4d, top). Clearly we are able to tune our system into a regime where the light-cone picture does not apply and significant amounts of information can propagate directly to distant neighbours. This is consistent with generalized Lieb–Robinson bounds for power laws, which for $\alpha < 1$ are trivial, placing no restriction on the speed of information propagation[6–8].

A quantitative analysis is provided by extracting the maximum quasiparticle group velocity v_g^{max} from the data (see Methods and Extended Data Fig. 4). For the shortest-range case, the observed v_g^{max} fits well with the nearest-neighbour case (Fig. 4d). As the interaction range is increased, the results are consistent with a divergence of v_g^{max}, as recently predicted[12]. Ultimately, the information propagation speed in our system is limited by the propagation of acoustic waves across the ion chain[21]. Note that, despite the faster-moving components in the longer-range data (Fig. 4c), the initial perturbation remains more localized. This is consistent with the predicted flattening of the dispersion relation away from the divergence. For a comparison of data with theory, see Extended Data Fig. 4.

Differences between the observed and ideal quantum dynamics following local quenches largely correspond to imperfect conservation of excitation number. This could be caused by electric field noise leading to heating of the ion's motional state or by unwanted spin–motion entanglement. For global quench dynamics, laser-frequency and magnetic-field fluctuations give rise to dephasing.

We have presented a new platform for investigating quantum phenomena—a many-body quantum system in which the states and properties of its quasiparticle excitations can be precisely initialized, controlled and measured. This opens many new paths for experimental investigations, the subjects of which can be broadly split into the following: (1) quantum transport phenomena, concerning how quantum states and entanglement[13], or excitations[14,27], propagate across quantum many-body systems; (2) how quantum systems reach equilibrium, including the question of when thermalization[15,28] and localization occur[16]; (3) entanglement growth and simulation complexity[17] (the interaction range parameter α is known to play a critical role in the growth rate of entanglement and the possibility of simulating the dynamics with conventional computers); and (4) quasiparticle behaviour near phase transitions[1]. For many of these research lines it would be useful, and feasible, to add localized spin excitation absorbers or reflective boundaries, and static or stochastically fluctuating disorder, to our system.

During the final stage of this work, we became aware of complementary recent work investigating global quenches of trapped-ion spin chains[26].

METHODS SUMMARY

Ions are held in a linear Paul trap, each encoding a spin-1/2 particle in the electronic states $|S_{1/2}, m = +1/2\rangle \equiv |\downarrow\rangle$ and $|D_{5/2}, m = +5/2\rangle \equiv |\uparrow\rangle$. Spins are manipulated with a narrow-linewidth laser at 729 nm (ref. 29). Ions are coherently manipulated with two laser beams intersecting the ion string perpendicularly from opposite directions. The first beam interacts with all the ions with nearly equal strength and is used for carrying out collective spin rotations, as well as implementing effective spin–spin interactions by means of electronic-state-dependent forces[3]. These forces off-resonantly drive the transverse motional modes of the ion string. The interaction range (α) is controlled by how far off-resonant the driving is and the axial trapping confinement. The second beam is strongly focused, steerable, and is used for single-spin rotations. Spatially resolved fluorescence measurements in conjunction with prior single-spin rotations allow us to take single-shot measurements of arbitrary spin correlations.

If our system had only nearest-neighbour interactions, the signal propagation after a local perturbation using σ_ℓ^x would be bounded by $|\langle\psi(t)|\mathcal{O}|\psi(t)\rangle - \langle\psi_0|\mathcal{O}|\psi_0\rangle| \leq 2||\mathcal{O}||I_d(4|t|\max_i(J_{i,i+1}))$, where $\mathcal{O}$ may be any local operator with norm $||\mathcal{O}||$ and distance d to the quench site ℓ. As Fig. 4d shows for $\mathcal{O} = \sigma_i^z$, this bound is only a

good approximation for the shortest-range case measured. Additionally, for nearest-neighbour interactions, the maximal group velocity $v_g^{\max}$ of magnon modes (that is, the largest slope of the quasiparticle dispersion relation) is finite. Figure 4a–c shows the corresponding light cone $t = d/v_g^{\max}$, outside which the signal would diminish exponentially if our system had only nearest-neighbour interactions. Clearly, longer-range interactions play an important role in our dynamics and must be taken into account.

Online Content Methods, along with any additional Extended Data display items and Source Data, are available in the online version of the paper; references unique to these sections appear only in the online paper.

Received 21 January; accepted 6 May 2014.

1. Sachdev, S. Quantum criticality: competing ground states in low dimensions. *Science* **288,** 475–480 (2000).
2. Calabrese, P. & Cardy, J. Time-dependence of correlation functions following a quantum quench. *Phys. Rev. Lett.* **96,** 136801 (2006).
3. Porras, D. & Cirac, J. I. Effective quantum spin systems with trapped ions. *Phys. Rev. Lett.* **92,** 207901 (2004).
4. Friedenauer, H., Schmitz, H., Glueckert, J., Porras, D. & Schaetz, T. Simulating a quantum magnet with trapped ions. *Nature Phys.* **4,** 757–761 (2008).
5. Lieb, E. & Robinson, D. The finite group velocity of quantum spin systems. *Commun. Math. Phys.* **28,** 251–257 (1972).
6. Cramer, M., Serafini, A. & Eisert, J. in *Quantum Information and Many Body Quantum Systems* (eds Ericsson, M. & Montangero, S.) 51 (Edizioni della Normale, 2008).
7. Hastings, M. B. in *Quantum Theory from Small to Large Scales, Lecture Notes of the Les Houches Summer School* (eds Frohlich, J., Salmhofer, M., Mastropietro, V., Roeck, W. D. & Cugliandolo, L.) Vol. 95, Ch. 5 (Oxford Univ. Press, 2010).
8. Nachtergaele, B. & Sims, R. Much ado about something: why Lieb-Robinson bounds are useful. *IAMP News Bull.* 22–29 (October 2010).
9. Cheneau, M. *et al.* Light-cone-like spreading of correlations in a quantum many-body system. *Nature* **481,** 484–487 (2012).
10. Fukuhara, T. *et al.* Microscopic observation of magnon bound states and their dynamics. *Nature* **502,** 76–79 (2013).
11. Langen, T., Geiger, R., Kuhnert, M., Rauer, B. & Schmiedmayer, J. Local emergence of thermal correlations in an isolated quantum many-body system. *Nature Phys.* **9,** 640–643 (2013).
12. Hauke, P. & Tagliacozzo, L. Spread of correlations in long-range interacting quantum systems. *Phys. Rev. Lett.* **111,** 207202 (2013).
13. Bose, S. Quantum communication through spin chain dynamics: an introductory overview. *Contemp. Phys.* **48,** 13–30 (2007).
14. Rebentrost, P., Mohseni, M., Kassal, I., Lloyd, S. & Aspuru-Guzik, A. Environment-assisted quantum transport. *New J. Phys.* **11,** 033003 (2009).
15. Rigol, M., Dunjko, V., Yurovsky, V. & Olshanii, M. Relaxation in a completely integrable many-body quantum system: an ab initio study of the dynamics of the highly excited states of 1D lattice hard-core bosons. *Phys. Rev. Lett.* **98,** 050405 (2007).
16. Yao, N. Y. *et al.* Many-body localization with dipoles. Preprint at http://arXiv.org/abs/1311.7151 (2014).
17. Schachenmayer, J., Lanyon, B. P., Roos, C. F. & Daley, A. J. Entanglement growth in quench dynamics with variable range interactions. *Phys. Rev. X* **3,** 031015 (2013).
18. Kitaev, A. Fault-tolerant quantum computation by anyons. *Ann. Phys.* **303,** 2–30 (2003).
19. Bravyi, S., Hastings, M. B. & Verstraete, F. Lieb-Robinson bounds and the generation of correlations and topological quantum order. *Phys. Rev. Lett.* **97,** 050401 (2006).
20. Eisert, J. & Osborne, T. General entanglement scaling laws from time evolution. *Phys. Rev. Lett.* **97,** 150404 (2006).
21. Jünemann, J., Cadarso, A., Perez-Garcia, D., Bermudez, A. & Garcia-Ripoll, J. Lieb-Robinson bounds for spin-boson lattice models and trapped ions. *Phys. Rev. Lett.* **111,** 230404 (2013).
22. Eisert, J., van den Worm, M., Manmana, S. R. & Kastner, M. Breakdown of quasi-locality in long-range quantum lattice models. *Phys. Rev. Lett.* **111,** 260401 (2013).
23. Kim, K. *et al.* Entanglement and tunable spin-spin couplings between trapped ions using multiple transverse modes. *Phys. Rev. Lett.* **103,** 120502 (2009).
24. Britton, J. W. *et al.* Engineered two-dimensional Ising interactions in a trapped-ion quantum simulator with hundreds of spins. *Nature* **484,** 489–492 (2012).
25. Islam, R. *et al.* Emergence and frustration of magnetism with variable-range interactions in a quantum simulator. *Science* **340,** 583–587 (2013).
26. Richerme, P. *et al.* Non-local propagation of correlations in long-range interacting quantum systems. *Nature* http://dx.doi.org/10.1038/nature13450 (this issue).
27. Plenio, M. B. & Huelga, S. F. Dephasing-assisted transport: quantum networks and biomolecules. *New J. Phys.* **10,** 113019 (2008).
28. Gong, Z.-X. & Duan, L.-M. Prethermalization and dynamical transition in an isolated trapped ion spin chain. *New J. Phys.* **15,** 113051 (2013).
29. Schindler, P. *et al.* A quantum information processor with trapped ions. *New J. Phys.* **15,** 123012 (2013).
30. Roos, C. F. *et al.* Bell states of atoms with ultralong lifetimes and their tomographic state analysis. *Phys. Rev. Lett.* **92,** 220402 (2004).

Acknowledgements We acknowledge discussions with L. Tagliacozzo, M. Heyl, A. Gorshkov and S. Bose. This work was supported by the Austrian Science Fund (FWF) under grant number P25354-N20, and by the European Commission via the integrated project SIQS and by the Institut für Quanteninformation. We also acknowledge support from the European Research Council through the CRYTERION Project (number 227959).

Author Contributions P.H., B.P.L. and C.F.R. developed the research, based on theoretical ideas conceived with P.Z.; P.J., B.P.L., C. H. and C.F.R. performed the experiments; B.P.L., P.J., C.F.R. and P.H. analysed the data and carried out numerical simulations. P.J., C.H., B.P.L., R.B. and C.F.R. contributed to the experiment; B.P.L., C.F.R., P.H., P.Z. and R.B. wrote the manuscript; all authors contributed to discussions of the results and of the manuscript.

Author Information Reprints and permissions information is available at www.nature.com/reprints. The authors declare no competing financial interests. Readers are welcome to comment on the online version of the paper. Correspondence and requests for materials should be addressed to C.F.R. (christian.roos@uibk.ac.at).

METHODS

Magnon eigenmodes. The dynamics in our system are well described by an *XY* Hamiltonian of *N* coupled spins,

$$H_{XY}=\hbar\sum_{i<j}J_{ij}\left(\sigma_i^+\sigma_j^-+\sigma_i^-\sigma_j^+\right) \quad (1)$$

where $\sigma_i^{\pm}=\left(\sigma_i^x\pm i\sigma_i^y\right)/2$, with $\sigma_i^{x,y}$ the usual Pauli matrices. We can use the Holstein–Primakoff transformation[31] to exactly map the spins to hard-core-interacting bosons, $\sigma_i^+\rightarrow a_i^\dagger,\sigma_i^-\rightarrow a_i$, where $a_i\left(a_i^\dagger\right)$ annihilates (creates) a boson on site *i*. The resulting model, $H_{\mathrm{boson}}=\hbar\sum_{i<j}J_{ij}\left(a_i^\dagger a_j+\mathrm{h.c.}\right)$, conserves the total number of particles (corresponding to conserved magnetization in the original spin model, allowing us to treat the transverse-field term $B\sum_i\sigma_i^z$ as a constant that we can neglect). In the single-particle subspace, diagonalizing H_{boson} is equivalent to diagonalizing the $N\times N$ matrix with entries J_{ij}. The result can be written in the form

$$H_{\mathrm{boson}}=\sum_k\hbar\omega_k a_k^\dagger a_k \quad (2)$$

where $a_k^\dagger=\sum_i c_{i,k}a_i^\dagger$ creates an excitation in eigenmode *k*. The mode functions $c_{i,k}$ are the normalized eigenvectors of J_{ij}. The eigenmode spectrum ω_k, that is, the dispersion relation, depends on the boundary conditions and interaction range. Once J_{ij} is known, it can be determined unambiguously. A single-particle wave-packet constructed from these eigenmodes is what we call a magnon quasiparticle.

A local perturbation of the fully polarized state, that is, a local quench, can be understood as the creation of a single magnon. After a spin flip at site ℓ, for example, the system state evolves according to

$$|\Psi(t)\rangle=e^{-iH_{\mathrm{boson}}t/\hbar}a_\ell^\dagger|0\rangle=\sum_k c_{\ell,k}^*e^{-i\omega_k t}a_k^\dagger|0\rangle \quad (3)$$

where $|0\rangle$ is the vacuum. When the number of excitations exceeds one, the picture of non- interacting magnons is only an approximation, and one has to account for the presence of hard-core interactions.

Calculation of group velocity. From equation (3), it becomes clear that the time evolution after creation of a single excitation is determined by the magnon dispersion relation, and consequently by the associated group velocities. For translationally invariant systems, the modes with energies ω_k are plane waves with well-defined wavevector *k*. In this case, the magnon group velocities are given by the well-known relation $v_g=\partial\omega/\partial k$. In contrast, for a finite system with open boundary conditions and nearest-neighbour interactions, the mode functions are standing waves of the form $c_i^{(k)}\propto\sin(k\cdot i)$, with $k=n\pi/(N+1)$, where $n=1\ldots N$ (we set the lattice spacing to unity). In the presence of finite-range interactions, the modes get distorted, but the number of nodes remains well defined. We can then still associate standing waves with the magnon modes and extract a maximal group velocity as: $v_g^{\max}\equiv|\max_k\left(\omega_{k+\pi/(N+1)}-\omega_k\right)(N+1)/\pi|$.

Encoding a spin-1/2 in an optical transition of a trapped ion. To experimentally realize the spin Hamiltonian H_{XY}, we identify the Zeeman states $|S_{1/2},m=+1/2\rangle$ and $|D_{5/2},\ m'=+5/2\rangle$ of $^{40}Ca^+$ with the $|\downarrow\rangle$ and $|\uparrow\rangle$ states of a spin-1/2 particle. The metastable $D_{5/2}$state has a lifetime of 1.16(2) s and is connected to the $S_{1/2}$ ground state by an electric quadrupole transition at a wavelength of $\lambda=729$ nm. The degeneracy of the ion's Zeeman states is lifted by a weak magnetic field of ≈4 G which allows us to initialize the $|S_{1/2},\ m=+1/2\rangle$ state using optical pumping techniques with a probability of about 99.9%. Choosing the $|D_{5/2},m'=+5/2\rangle$ state for encoding $|\uparrow\rangle$ has the advantage that spontaneous decay of the metastable state does not give rise to population loss from the computational state space. The static electric fields of the linear trap used to confine the ions axially induce electric quadrupole shifts which shift the energy of the $|\uparrow\rangle$ state. Hence, the transition frequency ω_0 between the spin states is slightly inhomogeneous across the ion string. However, for our experimental parameters, these inhomogeneities are below 20 Hz and thus considerably smaller than the spin–spin coupling strength.

Realization of variable-range spin–spin couplings in $^{40}Ca^+$. Variable-range spin–spin interaction of the Ising type are realized by globally addressing the ions with a laser beam whose direction is orthogonal to the ion string axis. The laser off-resonantly couples the ions' electronic states representing $|\downarrow\rangle$ and $|\uparrow\rangle$ to the ion strings' collective modes of motion in the directions perpendicular to the string. The laser carries two frequencies $\omega_\pm=\omega_0\pm\Delta$, which induces a Mølmer-Sørensen type interaction[32] by coupling to all first-order sidebands of the transverse collective modes of motion ($\hbar\omega_0$ is the energy difference between $|\downarrow\rangle$ and $|\uparrow\rangle$). In the limit of weak coupling, the induced effective interaction between the spins is described by the Hamiltonian[3,23]

$$H=\hbar\sum_{i<j}J_{ij}\sigma_i^x\sigma_j^x \quad (4)$$

with spin–spin coupling constants:

$$J_{ij}=\Omega_i\Omega_j\frac{\hbar k^2}{2m}\sum_n\frac{b_{i,n}b_{j,n}}{\Delta^2-\nu_n^2} \quad (5)$$

Here, Ω_i denotes the Rabi frequency of each component of the bichromatic beam on ion $i=1\ldots N$, $k=2\pi/\lambda$ and *m* is the ion mass. The summation runs over all $2N$ transverse modes, where ν_n is the mode's oscillation frequency and $b_{i,n}$ is the Lamb–Dicke factor, which is proportional to the displacement of the *i*th ion in the *n*th collective mode.

When the laser detuning Δ is set to a value higher than the frequency of the highest transverse mode, the coupling becomes anti-ferromagnetic with a range that is described approximately by a power-law dependence, $J_{ij}\propto|i-j|^{-\alpha}$. The exponent α can be varied between 0 and 3. The more similar the denominators in equation (5) become, the shorter the range of the interaction gets. This can be achieved by either increasing the laser detuning or by bunching up the transverse modes in frequency space by trapping the ions in a strongly anisotropic potential. In contrast to experiments engineering spin–spin interactions in trapped ions using Raman transitions connecting hyperfine states[4,23,24], our experiment uses a single-photon transition.

In all experiments presented here, with the exception of the data shown in Fig. 4a, we trap ions in a harmonic potential with an axial frequency of 219 kHz and transverse frequencies of 2.655 and 2.628 MHz. The degeneracy of the transverse frequencies is slightly lifted to achieve efficient Doppler cooling. The detuning Δ of the laser from the highest transverse mode is in the range of 15 to 120 kHz. To achieve $\alpha=1.41$ in a 15-ion string (Fig. 4a), we lowered the axial confinement to 150 kHz.

To reduce off-resonant excitation of the vibrational modes, frequency resolved sideband cooling of all radial vibrational modes to the ground state is employed at the beginning of each experiment. Rabi frequencies of $\Omega\approx(2\pi)125$ kHz are achieved by focusing about 20 mW of light to an elliptical Gaussian beam focus with beam waists $w_{||}=380$ μm and $w_\perp=33$ μm. In the seven-ion experiments, the intensity on the outer ions is about 8% lower than on the central ion. In the fifteen-ion experiment, this number increases to about 20%.

Implementation of the transverse field and its effect on the quantum dynamics. A transverse field $\hbar B\sum_i\sigma_i^z$ can be added to equation (4) by shifting both frequency components of the bichromatic beam by an additional amount $\delta=2B$, that is, the two frequencies are now $\omega_0\pm\Delta+2B$. The effect is to tune the $|\downarrow\rangle|\downarrow\rangle$ to $|\uparrow\rangle|\uparrow\rangle$ transition out of resonance whereas the $|\downarrow\rangle|\uparrow\rangle$ to $|\uparrow\rangle|\downarrow\rangle$ coupling is not affected as it is driven by absorption and stimulated emission of photons of the same wavelength.

If $B\gg J_{ij}$, joint spin flips coupling $|\downarrow\rangle|\downarrow\rangle\leftrightarrow|\uparrow\rangle|\uparrow\rangle$ are suppressed. All local quench experiments presented in this Letter were carried out in this regime where the number of excited spins is a conserved quantity. As dephasing due to magnetic field and laser noise is suppressed in subspaces with fixed numbers of excitations, the spin–spin dynamics can be followed over timescales of tens of milliseconds.

Compensation of a.c.-Stark shifts. Excitation of the $S_{1/2}\leftrightarrow D_{5/2}$ quadrupole transition by the laser inducing the spin–spin interactions gives rise to a.c.-Stark shifts of the coupled levels. These shifts are caused by off-resonant excitation of dipole transitions coupling the $S_{1/2}$ and $P_{1/2}$ states to other excited states. For our experimental parameters, the light shifts are of the order of 2–3 kHz. Moreover, they vary from one ion to the other, reflecting the intensity inhomogeneities of the laser beam used to drive the interactions. To compensate the a.c.-Stark shifts, a third laser frequency is added to the bichromatic beam causing a light shift of the same strength but opposite sign[33]. In order to keep the power of the compensating light field low, we chose to add a frequency component red-detuned by about 1 MHz from the $|\downarrow\rangle\leftrightarrow|\uparrow\rangle$ transition. For this method to work, care has to be taken that there are no polarization or *k*-vector gradients across the ion string that might introduce intensity-independent coupling strength variations among different ions. The intensity of this frequency component is set to the right value by analysing at which detuning of the bichromatic beam correlated spin flips are observed.

Single-ion addressing and state read-out. Addressing of single ions is achieved by a strongly focused beam inducing a light shift on one of the ions in the string. The beam position can be switched within 12 μs from one ion to any other ion using an acousto-optic deflector. Arbitrary single-ion rotations can be built up from operations combining single-ion a.c.-Stark shifts with global interactions resonantly coupling the states $|\downarrow\rangle$ and $|\uparrow\rangle$ (ref. 29). Combining these arbitrary single-ion rotations with spatially resolved detection of the ions' fluorescence on an EMCCD camera enables us to measure any observable that can be written as a tensor product of Pauli spin operators.

Quantum state tomography and entanglement quantification. For measurement of the entanglement of spin-pairs to the left and right of the central spin (Fig. 3),

we carry out quantum state tomography of each pair of spins. All required expectation values of two-spin observables $\sigma_i^{\beta_i}\sigma_j^{\beta_j}(\beta=x,y,z)$ can be estimated from measurements in nine different measurement bases where ions 1–3 are projected onto the same set of basis states and ions 4–7 onto the states of a different measurement basis. We estimate each expectation value by measuring 400 times in the corresponding basis, leading to a statistical uncertainty in each assigned value. We use the method of maximum-likelihood estimation[34] to find the most likely physical two-spin quantum state to have produced the observed set of estimated expectation values.

From the maximum-likelihood reconstructed two-spin density matrix we can calculate any one- or two-qubit property, such as entropy or concurrence. To translate the experimental uncertainties in expectation values into uncertainties in quantities derived from the reconstructed density matrix, we use the Monte Carlo bootstrapping technique[30].

To quantify the entanglement between pairs of spins with density matrix ρ we use the concurrence $C(\rho)$ — a widely used absolute entanglement measure for mixed and pure states of a two qubit system[35]:

$$C(\rho) \equiv \max(0, \lambda_1 - \lambda_2 - \lambda_3 - \lambda_4) \tag{6}$$

where λ_i are the eigenvalues in decreasing order of the Hermitian matrix $R \equiv \sqrt{\sqrt{\rho}(\sigma_y \otimes \sigma_y)\rho^*(\sigma_y \otimes \sigma_y)}\sqrt{\rho}$. The concurrence is a measure ranging from zero for a completely separable state up to one for a maximally entangled Bell state. Consequently, up to statistical uncertainty, a non-zero value of concurrence proves the existence of entanglement.

Measurement of spin–spin coupling matrix elements. For the measurement of the spin–spin coupling matrix J_{ij}, the ions are initially prepared in $|\downarrow\rangle$ by optical pumping. Next, all ions except i and j are transferred into an auxiliary Zeeman $D_{5/2}$ state, which does not couple to the bichromatic beam inducing the spin–spin coupling, and the state of one of the ions still remaining in $|\downarrow\rangle$ is flipped to $|\uparrow\rangle$. Finally, we switch on the bichromatic beam coupling $|\downarrow\rangle_i|\uparrow\rangle_j$ to $|\uparrow\rangle_i|\downarrow\rangle_j$ and measure the frequency of oscillation at which the two ions exchange the shared excitation.

Estimation of α from a dispersion relation. The spatial behaviour of the spin–spin couplings J_{ij} does not follow a perfect power law, making it difficult to extract an unambiguous exponent α from a direct fit in real space. However, the magnon dispersion relation allows us to estimate an effective value for α. To do this, we compare the dispersion relation of a system with power-law interactions to the dispersion relation of a realistic system obeying the experimental parameters. The power-law exponent α yielding the best fit provides an estimate for the interaction range. As seen in Fig. 1c, there is a close agreement between the dispersion relation from power-law interactions, the one simulated using experimental parameters, and the one using the measured coupling strengths. The corresponding value of α allows us to classify the system behaviour, since the dispersion relation uniquely determines the dynamics in the single-magnon subspace, see equation (3). Indeed, as demonstrated in Extended Data Fig. 1, simulations employing the estimated α reproduce the main features of the measured magnetization dynamics well, thus justifying its use. While the results for α of direct fits to the interactions depend on the details of the fit (using averaged interactions, interactions of the central spin, and so on), they typically agree within 20% with our values extracted from the quasiparticle spectrum. In particular, the regimes in which the extracted α fall—strong long-range ($\alpha<1$) or weak long-range ($\alpha>1$)—do not depend on the details of the method used.

Numerical simulations of the spin dynamics. For numerical simulations, we use the measured trap frequencies and the intensity distribution of the ions across the string to calculate the spin–spin coupling matrix J_{ij} .The coupling matrix and the measured laser–ion detuning are then used in a numerical integration of the equation of motion within the 2^N- dimensional Hilbert space describing the spin system. For the simulation of the fifteen-ion experiments, we disregarded processes not conserving the spin excitation number in order to carry out the numerical integration within the one-excitation subspace. The only free parameter in the simulations is the overall intensity of the bichromatic laser field which could not be calibrated perfectly (deviations from the measured value were always below 5%).

Approximate light cones and the Lieb–Robinson bound. If interactions in a quantum many-body system are of short range (for example, exponentially decreasing with distance), information cannot propagate arbitrarily fast. Therefore, when measuring an observable (such as the magnetization $\langle\sigma_i^z\rangle$) at a distance $d>0$ from a local perturbation, the observed expectation value can change only after a certain time. A mathematically rigorous formulation of this concept, which we will sketch now, was first given by Lieb and Robinson[5] and later generalized by various authors (see, for example, refs 6, 36, 37).

We denote the unperturbed initial state by $|\psi_0\rangle$ and by $|\psi(t)\rangle$ the state that has evolved during time t following the perturbation. Although the concept is more general, for consistency with Fig. 4, we consider a local perturbation with σ_ℓ^x, $\ell=(N+1)/2$, that is, $|\psi(t=0)\rangle=\sigma_\ell^x|\psi_0\rangle$. The change of any observable $\mathcal{O}$ can then be bounded by

$$|\langle\psi(t)|\mathcal{O}|\psi(t)\rangle - \langle\psi_0|\mathcal{O}|\psi_0\rangle| \le \left\|\left[\mathcal{O}(t),\sigma_\ell^x(0)\right]\right\| \tag{7}$$

where $\mathcal{O}(t)$ is the observable $\mathcal{O}$ evolved in the Heisenberg picture of the unperturbed Hamiltonian, and where $||\mathcal{O}||$ is the operator norm of $\mathcal{O}$, that is, the largest absolute value of its eigenvalues. The commutator on the right hand side quantifies how much it matters in which temporal order the operators $\mathcal{O}$ and σ_ℓ^x are applied.

If interactions decrease exponentially with distance, one can bound this commutator by[7,8]

$$\left\|\left[\mathcal{O}(t),\sigma_\ell^x(0)\right]\right\| \le \|\mathcal{O}\|F(d,t),\ F(d,t)=Ce^{\mu(v|t|-d)} \tag{8}$$

where C and μ are positive constants that depend on the interactions and lattice structure, and v is the so called Lieb–Robinson velocity. In essence, the function $F(d,t)$ provides an approximate light cone—information propagating faster than v is exponentially suppressed. The constants that appear in equation (8) are not unique[7,8], but as a reasonable choice one may identify the Lieb–Robinson velocity with the maximal group velocity $v_g^{\max}$. To estimate how strong the influence of interactions beyond nearest neighbours is in our system, we include in Fig. 4a–c the line $t=d/v_g^{\max}$, which would delineate the light cone in a system with only nearest-neighbour interactions. We compare our data to two opposite cases, one where interactions are simply truncated to nearest neighbours (homogenized over the chain, that is, interactions have strength $\bar{J}\equiv\frac{1}{N-1}\sum_{i=1}^{N-1}J_{i,i+1}$). The second case considers a nearest-neighbour model with interactions renormalized by the algebraic tail, that is, we replace all interactions by $\sum_{j>i_c}J_{j,i_c}$ where we use the value of the central ion $i_c=8$. For small α, the first magnon maximum clearly propagates faster than these nearest-neighbour light cones, demonstrating that effective nearest-neighbour models are insufficient—we have to account for the full long-range interaction to describe the quasiparticle propagation.

To quantify the deviation from short-range physics, we study in Fig. 4d the Lieb-Robinson bound, equation (8), for which one can find a compact formulation in the case of nearest-neighbour interactions. Given Hamiltonian $H=\sum_i h_{i,i+1}$, following ref. 19, one can bound $F(d,t)=\sum_{m=d}^{\infty}\mathcal{N}(m)(2g|t|/\hbar)^m/m!$ with $g=\max_i h_{i,i+1}$. Here, $\mathcal{N}(m)$ is the number of paths with length m that connect the quenched site ℓ to the observable $\mathcal{O}$ at a distance d. In one dimension, simple counting gives $\mathcal{N}(m)=\binom{m}{(m-d)/2}$ if either m and d are both even or both odd, and $\mathcal{N}(m)=0$ otherwise. Using this property, one can analytically evaluate the sum in $F(d,t)$ which takes the compact form

$$\left\|\left[\mathcal{O}(t),\sigma_\ell^x(0)\right]\right\| \le \|\mathcal{O}\|F(d,t),\ F(d,t)=2I_d(4g|t|/\hbar) \tag{9}$$

where $I_d(x)$ is the modified Bessel function of the first kind. In Fig. 4d we study the corresponding bound for $\mathcal{O}=\sigma_i^z$ and the renormalized interactions $g=\sum_{j>i_c}J_{j,i_c}$, showing that the nearest-neighbour Lieb–Robinson bound is only a good approximation for the shortest-range case measured. The longer-range cases can be captured by Lieb–Robinson bounds that take the long-range tail explicitly into account, and which cannot be characterized by a finite propagation velocity[6–8].

31. Holstein, T. & Primakoff, H. Field dependence of the intrinsic domain magnetization of a ferromagnet. *Phys. Rev.* **58,** 1098–1113 (1940).
32. Sørensen, A. & Mølmer, K. Quantum computation with ions in thermal motion. *Phys. Rev. Lett.* **82,** 1971–1974 (1999).
33. Häffner, H. *et al.* Precision measurement and compensation of optical Stark shifts for an ion-trap quantum processor. *Phys. Rev. Lett.* **90,** 143602 (2003).
34. James, D. F. V., Kwiat, P. G., Munro, W. J. & White, A. G. Measurement of qubits. *Phys. Rev. A* **64,** 052312 (2001).
35. Wootters, W. K. Entanglement of formation of an arbitrary state of two qubits. *Phys. Rev. Lett.* **80,** 2245–2248 (1998).
36. Hastings, M. B. Lieb-Schultz-Mattis in higher dimensions. *Phys. Rev. B* **69,** 104431 (2004).
37. Nachtergaele, B. & Sims, R. Lieb-Robinson bounds and the exponential clustering theorem. *Commun. Math. Phys.* **265,** 119–130 (2006).

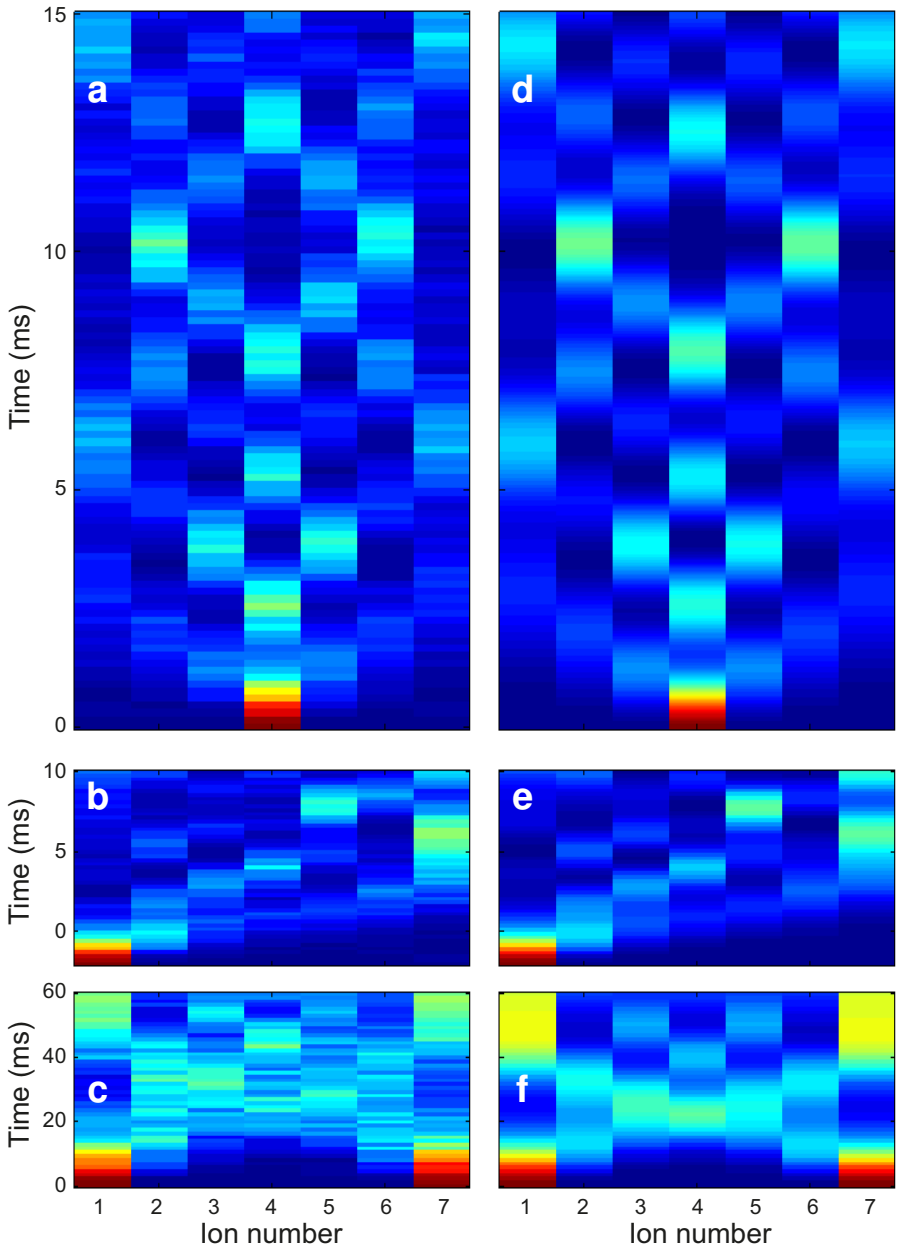

Extended Data Figure 1 | Quantum dynamics following local quenches in a seven-ion (seven-spin) system. **a**–**c**, Time evolution of the spatially resolved magnetization $\langle \sigma_i^z(t) \rangle$ (colour coded as in Fig. 2) for three different local quenches. In each panel measured data (left-hand side) is shown next to theoretical calculations for the ideal case (right-hand side). **a** and **d**, Quench at the centre spin, $\alpha \approx 1.36$; **b** and **e**, quench at the leftmost spin, $\alpha \approx 1.36$; **c** and **f**, quench at both ends of the chain, $\alpha \approx 1.75$. Theoretical calculations employ measured laser–ion coupling strengths and distribution across the ion chain.

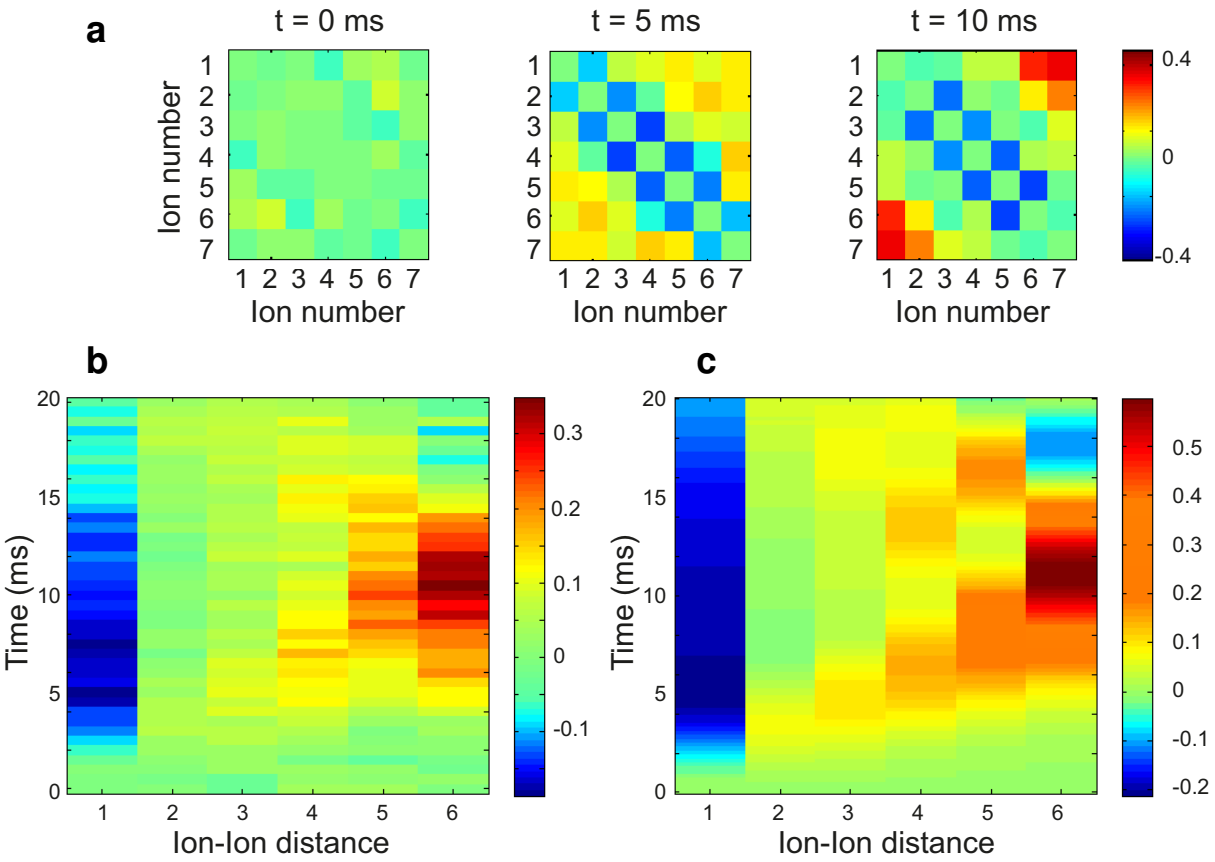

Extended Data Figure 2 | Quantum dynamics following a global quench in a seven-ion (seven-spin) system. **a**, Measured correlation matrices with elements $C_{i,j}(t) = \langle \sigma_i^z(t)\sigma_j^z(t)\rangle - \langle \sigma_i^z(t)\rangle\langle \sigma_j^z(t)\rangle$ (colour coded) at $t = 0$ ms, 5 ms, and 10 ms ($\alpha \approx 1.75$). **b**, Measured average magnetic spin–spin correlations $\overline{C}_n = \frac{1}{N-n}\sum_{i}^{N-n} C_{i,i+n}(t)$ (colour coded) as a function of time and distance n where the average was taken over all spin pairs (i, j) with $|i-j| = n$. **c**, Calculated spin–spin correlations $\overline{C}_n(t)$ (colour code: note the different colour scale) as a function of time and distance.

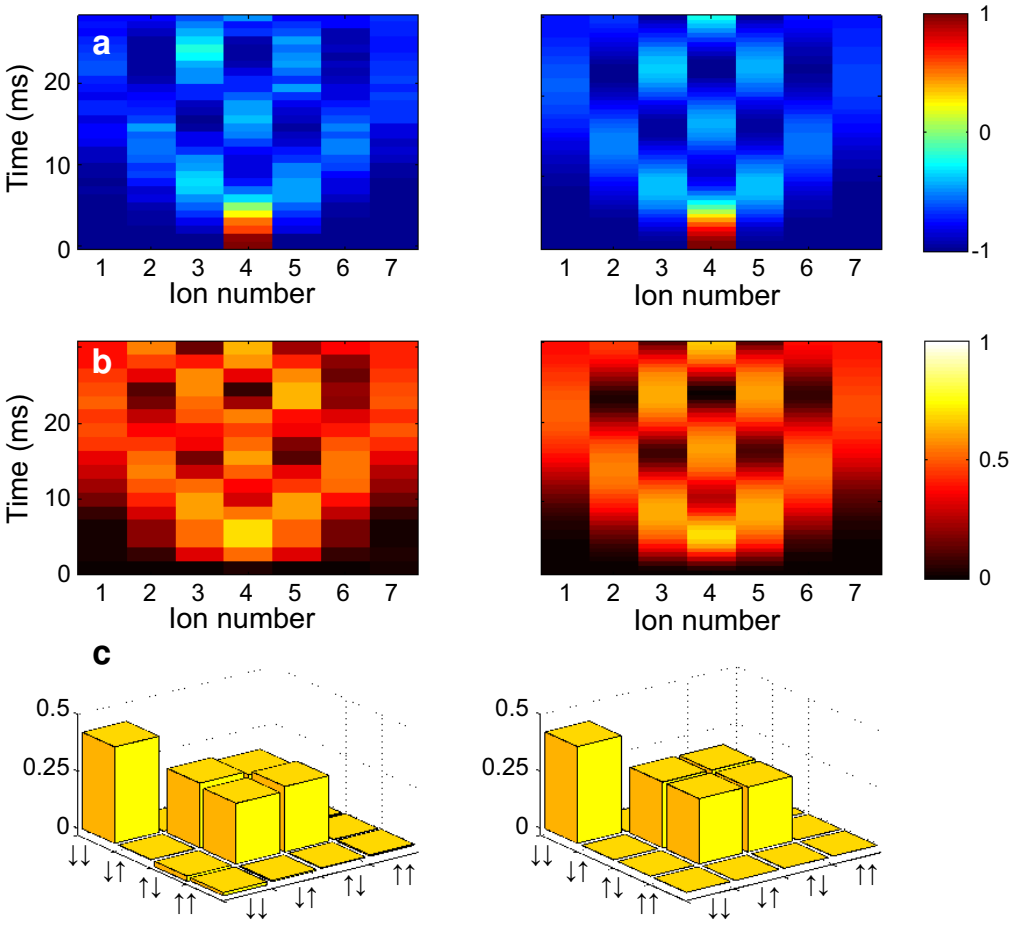

Extended Data Figure 3 | Entanglement distributed by quasiparticles. Following a quench of the central spin with short-range interactions ($\alpha \approx 1.75$), a distinct wavefront emerges. Each panel shows data (left-hand side) and theory (right-hand side) **a**, Measured single-spin magnetization (colour coded as in Fig. 2). **b**, Single-spin von Neumann entropy $-\mathrm{Tr}(\rho\log(\rho))$ normalized to one, derived from measured density matrices. Zero would correspond to a fully pure quantum state (black) and one (white) to a fully mixed state. The increase in entropy of any individual spin during the dynamics reflects the generation of entanglement with other spins. **c**, Real part of the tomographically reconstructed full density matrix of spins 3 and 5 at a time 9 ms after the quench. Imaginary parts are less than 0.03. The fidelity between the full experimentally reconstructed ρ and ideal state $|\psi\rangle$ is $F = 0.975 \pm 0.005$, using $F = \mathrm{Tr}(\rho|\psi\rangle\langle\psi|)$.

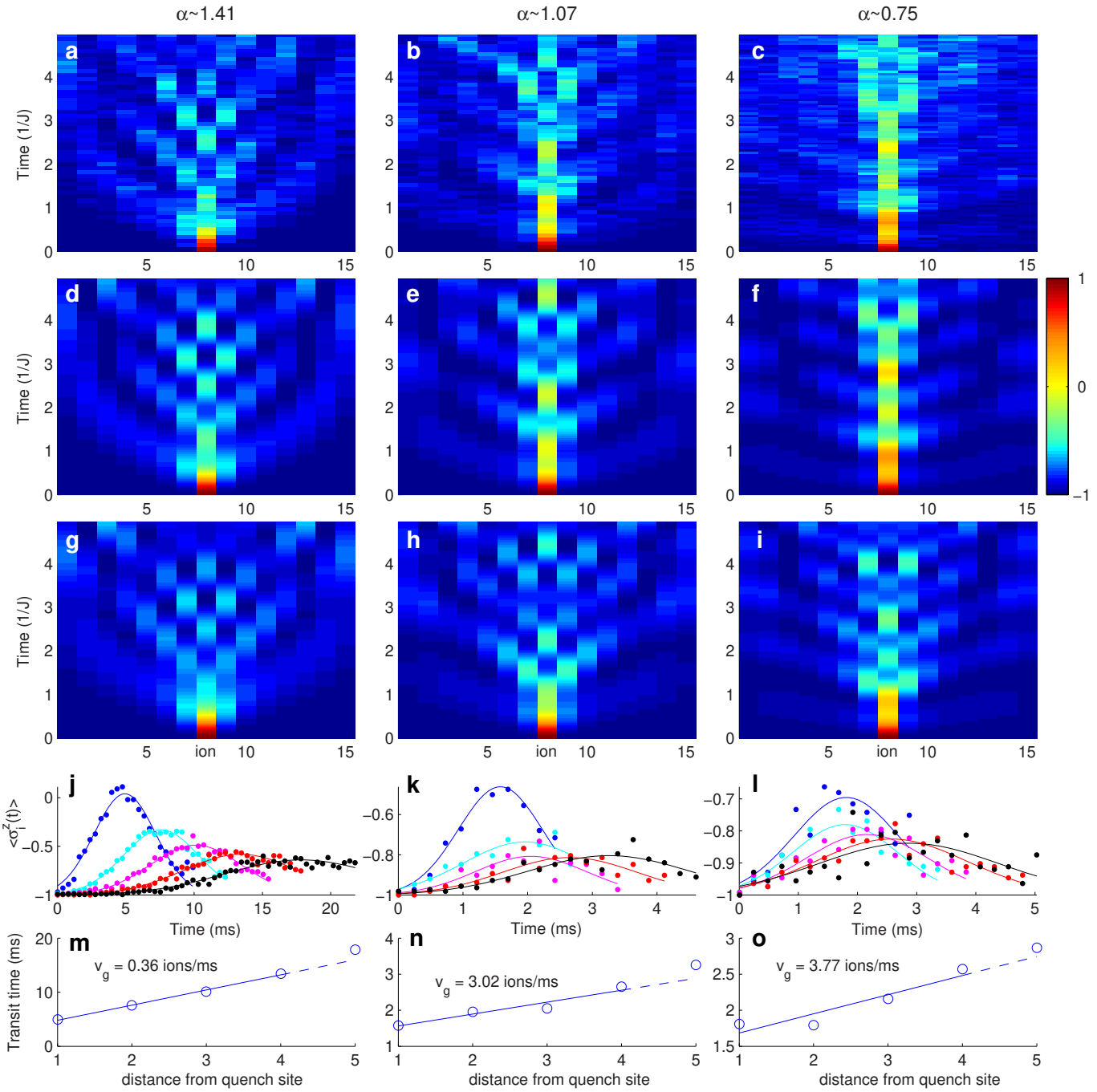

Extended Data Figure 4 | Quantum dynamics following a local quench in a 15-ion (15-spin) system. **a–c**, Experimentally measured time evolution of $\langle \sigma_i^z(t) \rangle$ (as in Fig. 4a–c). **d–f**, Theoretical calculations based on a measured spin–spin interaction matrix (such as presented in Fig. 1b). **h–i**, Theoretical calculations using $J_{ij} = \bar{J}/|i-j|^{\alpha}$, with $\bar{J} = \frac{1}{N-1}\sum_{i=1}^{N-1} J_{i,i+1}$ and α extracted from a fit to the measured dispersion relation. All theory calculations are done in the single-excitation subspace. **j–l**, Magnetization of symmetric pairs around the centre ion as a function of time: blue, ions 7 and 9; cyan, ions 6 and 10; purple, ions 5 and 11); red, ions 4 and 12; black, ions 3 and 13. The dashed lines are Gaussian fits to the measured arrival time of the first quasiparticle maximum (from **a–c**). **m–o**, Excluding the outermost ion to reduce finite-size effects, the fitted measured arrival maxima (circles) trace approximately a straight line when plotted against distance from quench site. A linear fit (solid line) yields an estimate for the propagation speed of the first quasiparticle maximum.

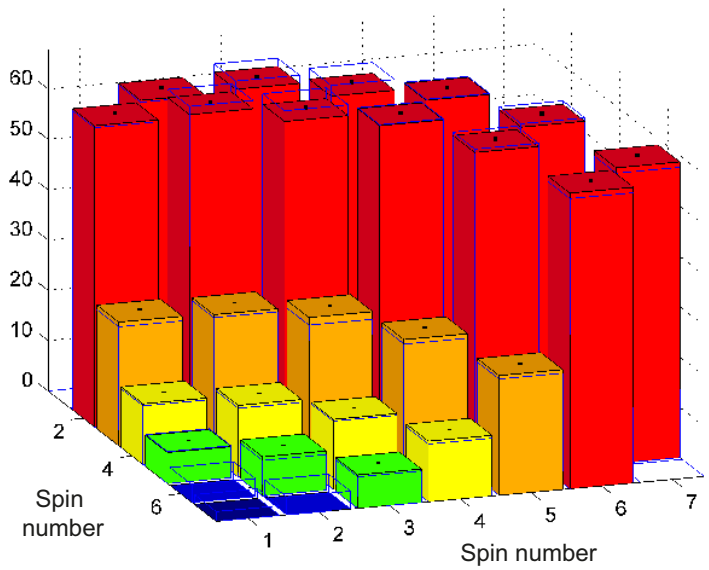

Extended Data Figure 5 | Example of a spin–spin interaction matrix J_{ij}. The plot compares theory and experiment. Each element of the J_{ij} matrix is measured directly (see Methods) in a system of $N = 7$ spins (solid coloured bars). Overlaid transparent bars with blue edges correspond to the results of a simulation which takes the following experimental parameters into account: the trapping frequencies; frequency of the bichromatic laser beams (see Methods); and measured individual laser–ion Rabi frequencies. The experimental data shown here are the same as in Fig. 1c. The elements J_{16}, J_{27} and J_{17} were not measured. Small black vertical lines show one standard deviation in the experimentally measured elements.